NANO LETTERS

pubs.acs.org/NanoLett

Letter

Unraveling the Growth Dynamics of Rutile $Sn_{1-x}Ge_xO_2$ Using Theory and Experiment

Fengdeng Liu, Nathan J. Szymanski, Kyle Noordhoek, Ho-sung Shin, Donghwan Kim, Christopher J. Bartel,* and Bharat Jalan*

Cite This: *Nano Lett.* 2025, 25, 299−305

Read Online

ACCESS | Metrics & More | Article Recommendations | Supporting Information

ABSTRACT: Rutile GeO_2 and related materials are attracting interest due to their ultrawide band gaps and potential for ambipolar doping in high-power electronic applications. This study examines the growth of rutile $Sn_{1-x}Ge_xO_2$ films through oxygen-plasma-assisted hybrid molecular beam epitaxy (hMBE). The film composition and thickness are evaluated across a range of growth conditions, with the outcomes rationalized by using density functional theory calculations. We find that up to 34% Ge can be successfully incorporated into $Sn_{1-x}Ge_xO_2$/r-Al_2O_3 ($x \leq 0.34$) at 600 °C. Our phase diagram calculations suggest that spinodal decomposition occurs at Ge concentrations exceeding 34%. However, the formation of a Ge-rich rutile phase is inhibited by amorphization of the Ge-rich film and volatility of GeO. We therefore speculate that maximizing the Ge content requires higher Ge flux and more oxidizing environments, providing insights into the growth mechanism of $Sn_{1-x}Ge_xO_2$ and paving the way toward the synthesis of pure rutile GeO_2 films.

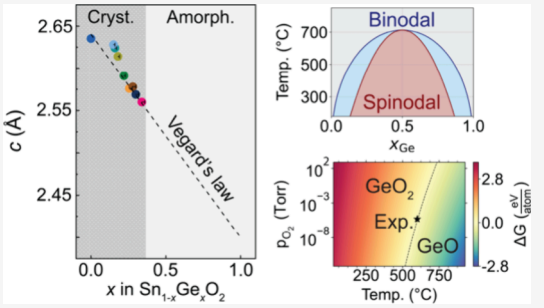

KEYWORDS: *GeO2, hybrid MBE, density functional theory calculations, growth dynamics*

In recent years, there has been growing interest in ultrawide band gap (UWBG) semiconductors for their potential applications in high-power electronics and deep-ultraviolet transparent conducting oxides.[1] Among the emerging UWBG materials, β-Ga_2O_3 has attracted the most attention due to its high electron mobility (184 $cm^2 V^{-1} s^{-1}$),[2] wide band gap (~5 eV),[3] and availability of compatible substrates. These properties have made β-Ga_2O_3 a robust platform for fundamental research in high-power devices, leading to significant progress in the field.[4−8] Nevertheless, β-Ga_2O_3 faces challenges that limit its further development. Its poor thermal conductivity[9] hampers effective heat dissipation, and it has a flat valence band[10] with localized polarons that restrict p-type doping. Alternative UWBG semiconducting materials must, therefore, be explored to overcome these challenges and advance next-generation power devices.

Rutile GeO_2 has recently emerged as a promising UWBG material with a band gap of 4.68 eV,[11] high predicted electron mobility of 244 $cm^2V^{-1} s^{-1}$ along the *c*-axis,[12] and good thermal conductivity of 51 W $m^{-1} K^{-1}$,[13] resulting in a higher Baliga figure of merit (BFOM) than β-Ga_2O_3. Rutile GeO_2 is also predicted to be amenable to ambipolar doping, thanks to its dispersive conduction and valence band structures.[14,15] However, its performance as a p-type semiconductor in optoelectronic devices may be limited by the trapping of hole polarons around acceptor dopants,[16,17] as well as the presence of a dipole-forbidden band gap.[11,17] High-quality rutile GeO_2 thin films need to be synthesized to further explore these properties. Several techniques, including pulsed laser deposition,[18] sputtering,[19] chemical vapor deposition (CVD),[20−23] and flux synthesis[24] have been successfully employed to synthesize rutile GeO_2. Molecular beam epitaxy (MBE), a well-suited thin film growth technique for exploring the growth mechanisms and surface kinetics based on precise control over the growth parameters and *in situ* monitoring capabilities, has also been investigated. Using this technique, the synthesis of pure rutile GeO_2 thin films has so far only been demonstrated via ozone-assisted MBE, where the desorption of GeO was identified as a key challenge.[25] Liu et al.[26] showed that rutile $Sn_{1-x}Ge_xO_2$(001) ($x \leq 54$ atom % and perovskite $SrSn_{1-y}Ge_yO_3$(001) (with $y \leq 16$ atom %) thin films could be synthesized using germanium tetraisopropoxide as the germanium source in oxygen plasma-assisted hybrid MBE (hMBE). Chen et al.[27] further studied the desorption of GeO from these films and established a growth window of GeO_2 defined by a specific range of temperatures and O/Ge flux ratios. Nevertheless, amorphization remains an issue, and further efforts are therefore needed to gain a comprehensive

Received: October 10, 2024
Revised: December 15, 2024
Accepted: December 18, 2024
Published: December 27, 2024

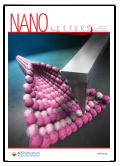

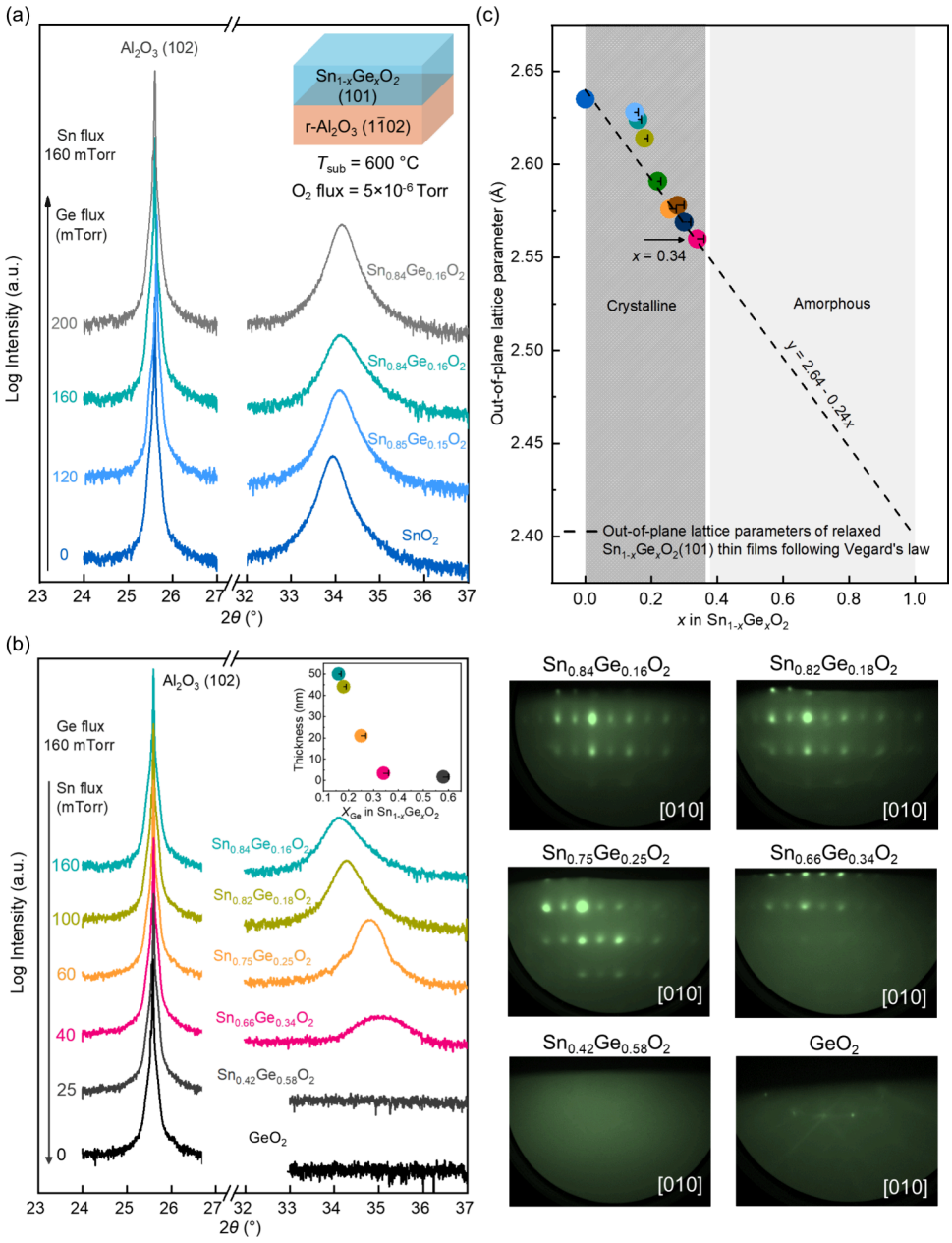

Figure 1. Characterization of rutile $Sn_{1-x}Ge_xO_2(101)$/r-$Al_2O_3(1\bar{1}02)$ thin films. (a) High resolution X-ray diffraction $2\theta-\omega$ coupled scans of $Sn_{1-x}Ge_xO_2$ (101)/r-Al_2O_3 ($1\bar{1}02$) thin films with varying HMDG(Ge) flux, keeping HMDT(Sn) flux constant. The inset shows the schematic of the sample structure. (b) High resolution X-ray diffraction $2\theta-\omega$ coupled scans and the corresponding RHEED patterns of $Sn_{1-x}Ge_xO_2$ (101)/r-Al_2O_3 ($1\bar{1}02$) thin films with varying HMDT(Sn) flux, keeping HMDG(Ge) flux constant. The inset shows the film thickness as a function of x_{Ge}. (c) Out-of-plane lattice parameter of $Sn_{1-x}Ge_xO_2(101)$ thin films with varying the x_{Ge}.

understanding of the factors that govern the formation of crystalline rutile GeO_2 in MBE.

In this article, we investigate the composition and growth mechanism of rutile $Sn_{1-x}Ge_xO_2$ thin films using hMBE as a model system. Whereas formation of pure rutile GeO_2 is limited by strong competition with a glassy phase, incorporating Sn is thought to favor crystallization.[25,28] Through a combination of experiments and density functional theory (DFT) calculations, it is shown that up to 34% Ge can be incorporated into $Sn_{1-x}Ge_xO_2$ at a substrate temperature of 600 °C. Attempts to synthesize films with a higher Ge content result in poor diffraction signals, indicating the absence of any crystalline phase. By modeling the vapor pressure above the film, we find that amorphization and GeO volatility preclude the formation of rutile $Sn_{1-x}Ge_xO_2$ in the Ge-rich regime. However, our results also suggest that these issues can potentially be avoided by using lower substrate temperature and/or higher oxygen flux to mitigate the volatility effect, thereby providing some guidance toward future efforts to synthesize rutile GeO_2 by using oxygen plasma-assisted hMBE.

We investigated the incorporation of Ge into SnO_2 by synthesizing $Sn_{1-x}Ge_xO_2$ (101)/r-Al_2O_3 ($1\bar{1}02$) using hMBE. Four experiments were performed with varied Ge flux between 0 and 200 mTorr while keeping the Sn flux fixed at 160 mTorr (as measured by a Baratron capacitance manometer; see the Methods section in the Supporting Information), and the corresponding beam equivalent pressures (BEPs) are listed in Table S1. Figure 1a shows high resolution X-ray diffraction

https://doi.org/10.1021/acs.nanolett.4c05043
Nano Lett. 2025, 25, 299−305

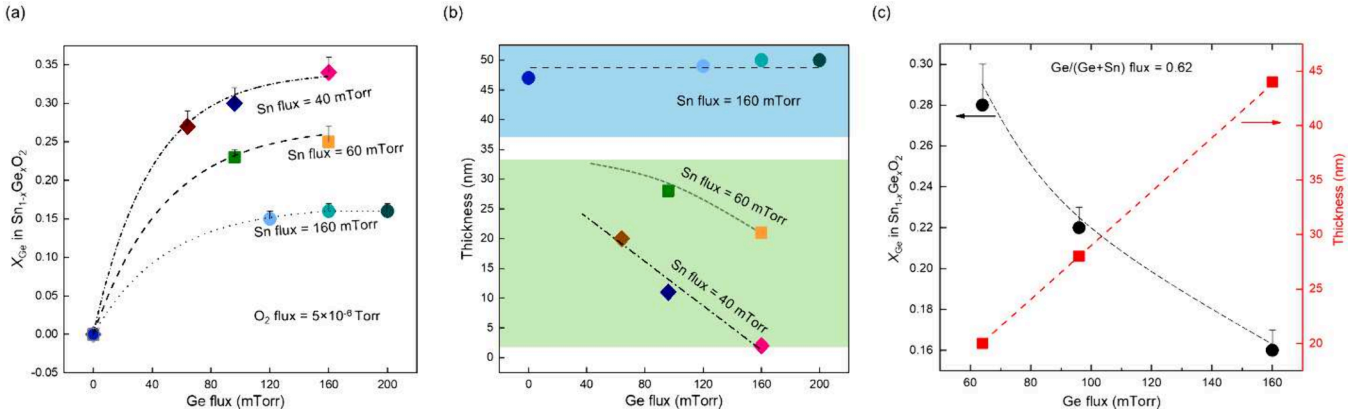

Figure 2. Analysis of $Sn_{1-x}Ge_xO_2$ films under different combination of Ge and Sn flux. (a) Measured Germanium concentration (x_{Ge}) in rutile $Sn_{1-x}Ge_xO_2$ films as a function of the input Ge and Sn fluxes at 600 °C. (b) Thickness of rutile $Sn_{1-x}Ge_xO_2$ films as a function of the input Ge and Sn fluxes. (c) x_{Ge} and thickness of rutile $Sn_{1-x}Ge_xO_2$ films as a function of Ge flux, keeping the oxygen flux and the flux ratio of Ge/(Sn+Ge) constant.

$2\theta-\omega$ coupled scans of the resulting films, and the inset shows the schematic of the sample structure. In the absence of a Ge flux (0 mTorr), we observe a clear rutile SnO_2 (101) film peak. As the Ge flux is increased from 0 to 120 mTorr, the film peak shifted toward higher 2θ indicating a decrease in the lattice parameter. This is consistent with the incorporation of Ge^{4+} ions, which have a smaller ionic radius (53 pm) compared to Sn^{4+} ions (69 pm). Indeed, X-ray photoelectron spectroscopy (XPS) revealed a Ge concentration of 15% in the film. Note that we also calculate the Ge concentration using the corrected relative sensitivity factors (RSF) from the built-in Multipak Spectrum software in the XPS setup, resulting in an error of approximately 1−2%, as shown in Table S2. However, we do not observe any further increase in the Ge content of the film when the Ge flux is increased from 120 to 200 mTorr.

To further increase the relative Ge content, we tested lower Sn fluxes (from 160 to 0 mTorr) while keeping the Ge flux fixed at 160 mTorr. As shown in Figure 1b, the Ge concentration of the film increases from 16% to 34% as the Sn flux is decreased from 160 to 40 mTorr. In contrast, attempts to further increase the Ge content by lowering the Sn flux to 25 mTorr resulted in an amorphous film with no diffraction signal, as shown by the RHEED pattern. Almost no GeO_2 film is deposited on the substrate in the absence of Sn flux, as indicated by the observation of the r-Al_2O_3 substrate RHEED pattern. The lack of crystallinity at high Ge concentrations is a consistent observation throughout our experiments. We also find that with an increased Ge concentration (from 16% to 34%), the root-mean-square (RMS) roughness of the films is reduced from 1465 to 665 pm, as shown by the AFM images in Figure S1, which may be related to a decrease in film thickness (inset of Figure 1b).[26] Figure 1c displays the out-of-plane lattice parameter of $Sn_{1-x}Ge_xO_2$ (101) extracted from $2\theta-\omega$ coupled scans with varied Ge content. For comparison, we also plot a dashed line that shows the out-of-plane lattice parameter that would be anticipated for ideal solid solutions of $Sn_{1-x}Ge_xO_2$ based on Vegard's law. The out-of-plane lattice parameters of the $Sn_{1-x}Ge_xO_2$ (x = 0.15, 0.16, and 0.18) films show a relatively large discrepancy from the calculated results, which can be attributed to errors in XPS measurements and the interpretation of broad film peaks in XRD. Nevertheless, the overall agreement between experimental and calculated results demonstrates that a wide range of Ge concentrations between 0% and 34% are accessible in $Sn_{1-x}Ge_xO_2$, but also that higher concentrations preclude the formation of a crystalline phase.

To gain additional insights into the growth of $Sn_{1-x}Ge_xO_2$, we performed a detailed analysis of the film composition and thickness with respect to the varied input fluxes. Figure 2a shows the measured Ge content as a function of Ge flux under different Sn fluxes (40, 60, and 160 mTorr). Each dashed line in this plot represents the trend in Ge content at fixed Sn flux. When the Sn flux is kept fixed, increasing the Ge flux consistently leads to higher Ge content until a plateau is reached. Interestingly, the Ge concentration where this plateau occurs depends on the Sn flux that is used—the limit ranges from 16% (for a Sn flux of 160 mTorr) to 34% Ge (for a Sn flux of 40 mTorr). While the appearance of a plateau in Ge content may be rationalized based on limited SnO_2-GeO_2 solubility (as detailed in the next section), the dependence of this limit on Sn flux is somewhat unexpected from equilibrium thermodynamics. We speculate that oxygen availability may play a role here, as the low amount of O_2 in the chamber (5×10^{-6} Torr) may be insufficient to support film growth when high Sn fluxes are used. However, we did not attempt to increase the oxygen background pressure in this work due to the restrictions of our MBE system, where a high oxygen pressure may lead to safety concerns and oxidation of other metal sources. Such low O_2 pressures also lead to more reducing conditions that favor GeO formation and subsequent desorption from the film, thereby reducing its overall Ge content. In contrast, Sn incorporation is less likely to be affected owing to the much lower vapor pressure of SnO.[29]

Figure 2b displays the measured film thickness as a function of Ge flux under different values of the constant Sn flux. We generally find that a higher Sn flux results in a higher growth rate, as evidenced by increased film thickness. This observation is consistent with previous reports of Sn-flux-limited growth at T_{sub} = 600 °C for pure SnO_2(101)/r-Al_2O_3.[30] In contrast, the film thickness is nearly independent of the Ge flux when high Sn fluxes are used. These findings suggest that much of the Sn is successfully incorporated into the film, whereas a large portion of the Ge is lost—e.g., to GeO volatility. As a result, increasing the Ge flux beyond a certain point does not contribute to increased film growth. On the contrary, increasing the Ge flux when the Sn flux is low (≤60 mTorr)

https://doi.org/10.1021/acs.nanolett.4c05043
Nano Lett. 2025, 25, 299−305

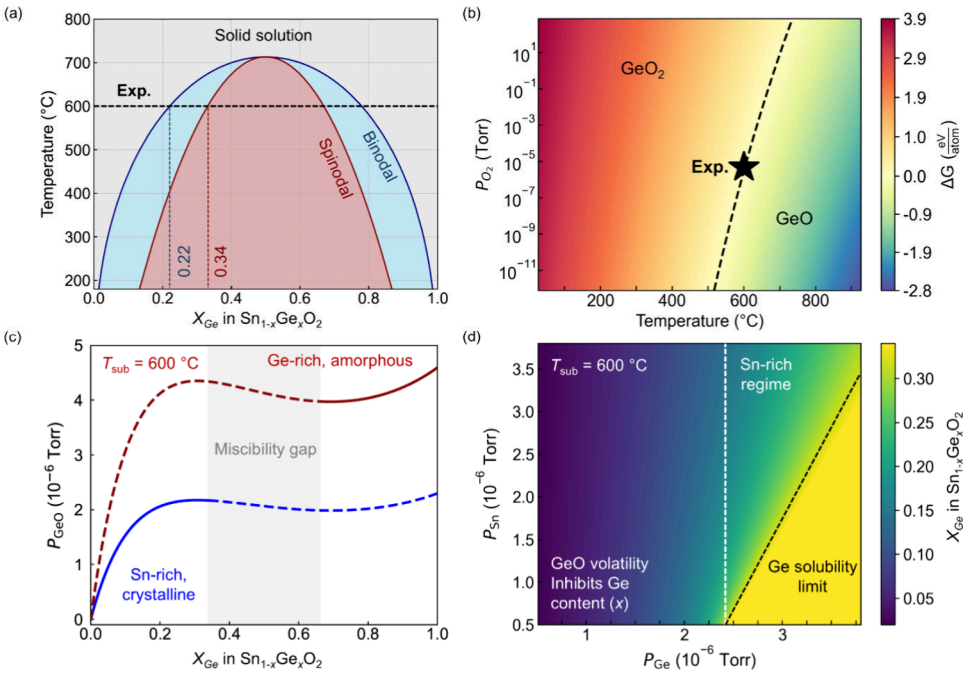

Figure 3. Modeling of $Sn_{1-x}Ge_xO_2$films. (a) The DFT-computed binary phase diagram between rutile SnO_2 (left) and GeO_2 (right). The (upper) blue line represents the binodal curve, while the (lower) red line represents the spinodal curve. (b) The change in the Gibbs free energy (ΔG) associated with GeO_2 decomposition into GeO and O_2 (both gases) is plotted as a function of temperature and oxygen partial pressure. (c) The vapor pressure of GeO above $Sn_{1-x}Ge_xO_2$ is plotted as a function of Ge content at 600 °C. The blue and red curves are obtained from crystalline (rutile) and amorphous solid solutions, respectively. These vapor pressures were obtained from previous experimental reports for GeO_2,[32,34] and a regular solution model was used to compute the change in vapor pressure with composition. (d) The predicted Ge concentration in $Sn_{1-x}Ge_xO_2$ is plotted as a function of the precursor (Ge and Sn) fluxes. The yellow region corresponds to the metastable limit of Ge solubility (34%) in SnO_2, as determined from our computed phase diagram.

leads to a decrease in film thickness. As will be discussed in the next section, these films are likely metastable with respect to phase segregation, and therefore, increasing the Ge flux within this metastable regime may lead to phase segregation and subsequent volatility of GeO. The increased formation and loss of GeO may also deplete the little O_2 that is available in the system, in turn decreasing the rate at which the oxide film can form.

To clarify the influence of the *total* (Sn + Ge) metal flux on the composition and thickness of $Sn_{1-x}Ge_xO_2$ films, Figure 2c illustrates both quantities as a function of Ge flux while keeping the flux ratio of Ge/(Ge + Sn) fixed at 0.62. The film thickness (red line) shows a linear increase with a higher cation flux, as more Ge and Sn are available to form $Sn_{1-x}Ge_xO_2$. In contrast, the Ge content decreases with higher cation flux, despite the ratio of Ge/(Ge + Sn) fluxes remaining unchanged. This result further points to the importance of oxygen availability and the effect it has on GeO formation. We speculate that by consuming much of the O_2 available in the chamber, higher metal fluxes lead to a more reducing environment that favors GeO formation and, therefore, decreases the Ge content in the film. These factors are investigated theoretically in the next few sections.

To rationalize the plateau in Ge content (≲34%) observed for all the films synthesized in this work, we studied the energetics of $Sn_{1-x}Ge_xO_2$ by performing DFT calculations on 19 special quasi-random structures (SQSs) with equally spaced compositions (x_{Ge} = 0.05, 0.10, ..., 0.90, 0.95). Ignoring pressure effects ($P\Delta V$) on the enthalpy term, which are negligible for most solids, the Gibbs free energy of mixing was calculated at each composition as follows:

$$\Delta G_{mix} = \Delta U_{mix} - T\Delta S_{mix} \quad (1)$$

where ΔU_{mix} is the change in the DFT-computed internal energy caused by mixing, T is the temperature, and ΔS_{mix} is the entropy change of mixing. The Sn and Ge atoms are assumed to distribute randomly on the cation sublattice, leading to an entropy change of

$$\Delta S_{mix} = -k_B[x_{Ge}\ln x_{Ge} + (1 - x_{Ge})\ln(1 - x_{Ge})] \quad (2)$$

The free energies obtained from these calculations were used to fit a regular solution model (see the Methods) of the binary phase diagram between rutile SnO_2 and GeO_2, shown in Figure 3a. The gray region (above both curves) represents conditions of complete solubility, the blue regions (below the binodal curve) represent conditions where the solid solution is metastable with respect to phase segregation, and the red region (below the spinodal curve) represents conditions where the solid solution is unstable with respect to spinodal decomposition. A miscibility gap is observed up to ~710 °C, above which SnO_2 and GeO_2 are predicted to be completely soluble. At 600 °C, the temperature that was used in our experiments, the equilibrium solubility limit of Ge in SnO_2 is only about 22%. Coincidentally, the predicted limit of metastable solubility at 600 °C reaches 34%, which agrees with the maximum Ge content that was obtained in a crystalline film ($Sn_{0.66}Ge_{0.34}O_2$). Such a close match between theory and experiment is not generally expected and should be taken with caution, but nonetheless supports the anticipated metastability of $Sn_{1-x}Ge_xO_2$ at moderate Ge concentrations. At concentrations greater than 34%, phase separation is much more likely to occur given that spinodal decomposition does

https://doi.org/10.1021/acs.nanolett.4c05043
Nano Lett. 2025, 25, 299−305

not require nucleation and growth. Attempts to exceed this limit (e.g., by using a high Ge flux) should, in principle, result in the formation of a Ge-rich secondary phase; however, this phase was never observed in our experiments. Its absence may be attributed to amorphization, GeO volatility, or a combination of both. These effects can be mitigated by improving the solubility between SnO_2 and GeO_2, as shown in our previous work where a Ge content of 56% was achieved through strain engineering on a $TiO_2(001)$ substrate;[26] however, the current study only used r-Al_2O_3 $(1\bar{1}02)$ substrates for the deposition of $Sn_{1-x}Ge_xO_2$, resulting in all relaxed thin films.

The formation of gaseous GeO has been reported to plague the deposition of Ge-containing oxides in MBE.[25,27] To investigate the prevalence of GeO formation in our system, we first study the thermodynamic driving force associated with the below reaction:

$$GeO_2(s) \rightarrow GeO(g) + \frac{1}{2}O_2(g) \tag{3}$$

The driving force behind this reaction is defined by the change in the Gibbs free energy (ΔG) as the reactants transform to the products under a given set of conditions (temperature and pressure). The temperature-dependent free energy of each phase in the above equation was acquired from previous experimental measurements,[31] and the pressure dependence of each gaseous free energy was computed under an ideal gas assumption ($\Delta\mu_i = RT \ln p_i$).

The driving force (ΔG) to form GeO is plotted as a function of temperature (T) and oxygen partial pressure (p_{O_2}) in Figure 3b. Red shades of color represent conditions where GeO_2 is stable ($\Delta G > 0$), while blue shades of color represent conditions where decomposition into GeO and O_2 is favored ($\Delta G < 0$). These results show that high temperatures and low oxygen partial pressures lead to more reducing conditions that favor gas formation, where GeO and O_2 are stabilized owing to their increased entropy. In contrast, low temperatures and high oxygen partial pressures stabilize the more enthalpically stable solid GeO_2 phase, which agrees with the reported pure rutile GeO_2 via ozone-assisted MBE.[25] Also shown in Figure 3b is a black star that signifies the conditions used in our experiments (T = 600 °C, $p_{O_2} \approx 5 \times 10^{-6}$ Torr), positioned very near the boundary that separates GeO_2 from GeO (black dashed line), which also provides support for our previous assumption that the growth condition does not favor the formation of pure rutile GeO_2. This highlights the prevalence of GeO volatility during the deposition of Ge-containing oxides, which will be strongly influenced by the film's composition, experimental conditions, and precursor fluxes.

To model the composition of $Sn_{1-x}Ge_xO_2$ films formed under specific conditions and fluxes, we assume that GeO and O_2 are the only two gases produced at appreciable rates. This assumption is justified by previous measurements that reveal GeO and O_2 have orders of magnitude larger vapor pressures above GeO_2 than SnO above SnO_2.[29] Recent work from Chae et al. has additionally shown that the flux of gaseous species from GeO_2 is much larger than that from SnO_2 at the same temperature.[25] We also assume that Ge and Sn have equal sticking coefficients on the substrate, although this sticking coefficient may not be unity—i.e., not all Sn or Ge atoms may be successfully incorporated, but their adsorption rates are comparable. The Ge content of the film (x_{Ge}) can then be calculated as the ratio of incident cation fluxes (p^0_{Ge}, p^0_{Sn}), adjusted for the outward flux of GeO (p_{GeO}):

$$x_{Ge} = \frac{p^0_{Ge} - p_{GeO}}{p^0_{Ge} + p^0_{Sn} - p_{GeO}} \tag{4}$$

When the film consists only of rutile GeO_2 (without Sn), the equilibrium vapor pressure of GeO is ~2.3×10^{-6} Torr at 600 °C.[32] However, this value will change with the incorporation of Sn. If $Sn_{1-x}Ge_xO_2$ were an ideal solution, the vapor pressure of GeO above it would simply be a linear interpolation of that above SnO_2 (0 Torr) and GeO_2 (2.3×10^{-6} Torr). In reality, there is an enthalpy of mixing between the two compounds that causes the vapor pressure to deviate from linearity. Our DFT calculations predict endothermic mixing ($\Delta H_{mix} > 0$) between SnO_2 and GeO_2, with an effective interaction parameter, Ω, of 0.17 eV/cation (see Methods). A regular solution model can then be used to predict the vapor pressure of GeO above the rutile $Sn_{1-x}Ge_xO_2$ as a function of x_{Ge}, which is shown by the blue curve in Figure 3c.

From the computed vapor pressure of GeO (p_{GeO}) as a function of Ge concentration in the film (x_{Ge}), we can solve eq 4 under various combinations of Ge and Sn pressures (p^0_{Ge}, p^0_{Sn}) at 600 °C. The resulting solutions are plotted in Figure 3d, where the heatmap illustrates the predicted Ge content of the resulting film. Here we assess a range of pressures that are comparable to experimentally measured values in the chamber, which are several orders of magnitude less than the nominal input fluxes (measured in the gas line). The plot in Figure 3d shows that at a fixed Sn pressure increasing the Ge pressure leads to a higher Ge content in the film. A plateau in the Ge content is observed at 34% at high Ge pressures (>2.3×10^{-6} Torr), which arises from the (metastable) limit of Ge solubility in SnO_2 (Figure 3b). Further increases in the Ge pressure should lead to spinodal decomposition whereby a Ge-rich secondary phase forms; however, this phase is more likely to be amorphous owing to the exceptional glass-forming ability of GeO_2.[33] Amorphization not only complicates the detection of this phase using diffraction but also leads to a near 2-fold increase in the vapor pressure of GeO above it.[34] To account for this effect, the vapor pressure of GeO above $Sn_{1-x}Ge_xO_2$ was recalculated (red line, Figure 3c) under the assumption that Ge-rich compositions ($x_{Ge} \geq 66\%$) are amorphous and therefore exhibit increased volatility. These calculations predict that no Ge-rich compositions will form under the range of pressures used in our experiments, as the rate at which GeO escapes the film exceeds the rate at which Ge is supplied to it. This leaves only a Sn-rich film, in agreement with our experimental observations.

While the Ge content of the film is most prominently affected by the Ge pressure, one may also vary the Sn pressure to control the resulting composition. As shown in Figure 3d, decreasing the Sn pressure at fixed Ge pressure leads to increased Ge concentrations in the film. This can be understood by examining eq 4, where lower Sn pressures result in a higher relative Ge content as a proportion of the total incident cation pressure. However, there is some trade-off between this effect and the growth rate of the film. As demonstrated in our experiments, decreasing the Sn flux at fixed Ge flux does indeed lead to an increase in the Ge content of the film, but doing so also reduces its thickness, given the decreased total cation flux. One may anticipate that a high Ge content and fast growth rates could be achieved by increasing

https://doi.org/10.1021/acs.nanolett.4c05043
Nano Lett. 2025, 25, 299−305

the overall cation flux while keeping the ratio of Ge/(Ge + Sn) fluxes constant. However, experiments suggest that this approach is ineffective, likely because oxygen availability becomes the limiting factor. If this is the case, then increasing the oxygen partial pressure may be an effective method to increase the growth rate while mitigating the volatility of GeO.

We have investigated the composition and thickness of $Sn_{1-x}Ge_xO_2$ (101)/r-Al_2O_3 ($1\bar{1}02$) thin films using hMBE. These experiments were supported via DFT calculations to understand the equilibrium thermodynamics and growth dynamics of $Sn_{1-x}Ge_xO_2$ grown at 600 °C. Our findings demonstrate that maximizing Ge content requires the use of high Ge fluxes and low Sn fluxes, though, even with these optimized fluxes, the Ge content plateaus at 34% before spinodal decomposition occurs. The Ge-rich phase resulting from decomposition instead forms an amorphous material that is highly susceptible to GeO volatility, preventing the successful synthesis of $Sn_{1-x}Ge_xO_2$ films with high Ge content. Considering these limitations, we propose that increased Ge concentrations may be achieved by 1) improving the solubility between SnO_2 and GeO_2 through strain engineering, thereby inhibiting spinodal decomposition by lowering the critical solution (i.e., the consolute) temperature; 2) using a lower synthesis temperature that discourages the formation of gaseous phases such as GeO; and 3) providing the chamber with a higher O_2 partial pressure that creates a more oxidizing environment, under which Ge^{4+} is thermodynamically preferred. These findings shed light on the factors that govern the synthesis of Ge-containing oxides in MBE, paving the way toward the formation of a pure rutile GeO_2 thin film.

■ ASSOCIATED CONTENT

Supporting Information

The Supporting Information is available free of charge at https://pubs.acs.org/doi/10.1021/acs.nanolett.4c05043.

Experimental section including film growth and film characterization, DFT calculations, the baratron pressures and BEPs of HMDG and HMDT precursors used in the synthesis process, XPS analysis of $Sn_{1-x}Ge_xO_2$ film compositions, and AFM images of $Sn_{1-x}Ge_xO_2$ films.

■ AUTHOR INFORMATION

Corresponding Authors

Christopher J. Bartel − *Department of Chemical Engineering and Materials Science, University of Minnesota-Twin Cities, Minneapolis, Minnesota 55455, United States;* orcid.org/0000-0002-5198-5036; Email: cbartel@umn.edu

Bharat Jalan − *Department of Chemical Engineering and Materials Science, University of Minnesota-Twin Cities, Minneapolis, Minnesota 55455, United States;* orcid.org/0000-0002-7940-0490; Email: bjalan@umn.edu

Authors

Fengdeng Liu − *Department of Chemical Engineering and Materials Science and Department of Electrical and Computer Engineering, University of Minnesota-Twin Cities, Minneapolis, Minnesota 55455, United States*

Nathan J. Szymanski − *Department of Chemical Engineering and Materials Science, University of Minnesota-Twin Cities, Minneapolis, Minnesota 55455, United States*

Kyle Noordhoek − *Department of Chemical Engineering and Materials Science, University of Minnesota-Twin Cities, Minneapolis, Minnesota 55455, United States;* orcid.org/0000-0002-1076-8799

Ho-sung Shin − *Department of Chemical Engineering and Materials Science, University of Minnesota-Twin Cities, Minneapolis, Minnesota 55455, United States;* orcid.org/0009-0004-3850-7015

Donghwan Kim − *Department of Chemical Engineering and Materials Science, University of Minnesota-Twin Cities, Minneapolis, Minnesota 55455, United States*

Complete contact information is available at: https://pubs.acs.org/10.1021/acs.nanolett.4c05043

Author Contributions

F.L., H.S. and B.J. designed experiments. Rutile films were grown and characterized by F.L., H.S. and D.K., N.S. and K.N performed DFT calculations under the direction of C.B. F.L. N.S., and K.N wrote the first draft of the manuscript with input from all authors. B.J. and C.B. directed and organized the experimental and theoretical aspects of the project, respectively.

Notes

The authors declare no competing financial interest.

■ ACKNOWLEDGMENTS

This work (F.L., H.S, B.J.) is supported primarily by the National Science Foundation (NSF) through the Future of Semiconductor (FuSe) grant under Award number DMR-2328702 and partially though the FuSe teaming grant (FuSe-TG) (Award number DMR-2235208). We (D.K. and B.J.) acknowledge partial support supported by the Air Force Office of Scientific Research (AFOSR) through Grants FA9550-21-1-0025 and FA9550-23-1-0247. Film growth was performed using instrumentation funded by AFOSR DURIP awards FA9550-18-1-0294 and FA9550-23-1-0085. C.B and B.J. received partial support from the UMN MRSEC program under Award No. DMR-2011401. K.N. was supported by the Department of Defense (DoD) through the National Defense Science & Engineering Graduate (NDSEG) Fellowship Program. Parts of this work were carried out in the Characterization Facility, University of Minnesota, which receives partial support from the NSF through the MRSEC (Award Number DMR-2011401) and the NNCI (Award Number ECCS-2025124) programs. Portions of this work were carried out at the Minnesota Nano Center, which receives support from the NSF through the National Nanotechnology Coordinated Infrastructure (NNCI) under Award No. ECCS-2025124. The authors acknowledge the Minnesota Supercomputing Institute (MSI) at the University of Minnesota for providing resources that contributed to the research results reported within this paper.

■ REFERENCES

(1) Tsao, J.; Chowdhury, S.; Hollis, M.; Jena, D.; Johnson, N.; Jones, K.; Kaplar, R.; Rajan, S.; Van de Walle, C.; Bellotti, E. Ultrawide-bandgap semiconductors: research opportunities and challenges. *Advanced Electronic Materials* **2018**, *4* (1), No. 1600501.

(2) Feng, Z.; Anhar Uddin Bhuiyan, A.; Karim, M. R.; Zhao, H. MOCVD homoepitaxy of Si-doped (010) β-Ga_2O_3 thin films with superior transport properties. *Appl. Phys. Lett.* **2019**, *114* (25), No. 250601.

(3) Zhang, J.; Willis, J.; Yang, Z.; Lian, X.; Chen, W.; Wang, L.-S.; Xu, X.; Lee, T.-L.; Chen, L.; Scanlon, D. O.; Zhang, K. H.L. Deep UV transparent conductive oxide thin films realized through degenerately

doped wide-bandgap gallium oxide. *Cell Reports Physical Science* **2022**, *3* (3), No. 100801.
(4) Galazka, Z.; Uecker, R.; Irmscher, K.; Albrecht, M.; Klimm, D.; Pietsch, M.; Brützam, M.; Bertram, R.; Ganschow, S.; Fornari, R. Czochralski growth and characterization of β-Ga_2O_3 single crystals. *Crystal Research and Technology* **2010**, *45* (12), 1229−1236.
(5) Higashiwaki, M.; Sasaki, K.; Murakami, H.; Kumagai, Y.; Koukitu, A.; Kuramata, A.; Masui, T.; Yamakoshi, S. Recent progress in Ga_2O_3 power devices. *Semicond. Sci. Technol.* **2016**, *31* (3), No. 034001.
(6) Peng, Y.; Zhang, Y.; Chen, Z.; Guo, D.; Zhang, X.; Li, P.; Wu, Z.; Tang, W. Arrays of Solar-Blind Ultraviolet Photodetector Based on β-Ga_2O_3 Epitaxial Thin Films. *IEEE Photonics Technology Letters* **2018**, *30* (11), 993−996.
(7) Zhang, J.; Shi, J.; Qi, D.-C.; Chen, L.; Zhang, K. H. Recent progress on the electronic structure, defect, and doping properties of Ga_2O_3. *Appl. Materials* **2020**, *8* (2), No. 020906.
(8) Green, A. J.; Speck, J.; Xing, G.; Moens, P.; Allerstam, F.; Gumaelius, K.; Neyer, T.; Arias-Purdue, A.; Mehrotra, V.; Kuramata, A.; et al. β-Gallium oxide power electronics. *Appl Materials* **2022**, *10* (2), No. 029201.
(9) Guo, Z.; Verma, A.; Wu, X.; Sun, F.; Hickman, A.; Masui, T.; Kuramata, A.; Higashiwaki, M.; Jena, D.; Luo, T. Anisotropic thermal conductivity in single crystal β-gallium oxide. *Appl. Phys. Lett.* **2015**, *106* (11), No. 111909.
(10) Varley, J. B.; Janotti, A.; Franchini, C.; Van de Walle, C. G. Role of self-trapping in luminescence and p-type conductivity of wide-band-gap oxides. *Physical Review B-Condensed Matter and Materials Physics* **2012**, *85* (8), No. 081109.
(11) Mengle, K. A.; Chae, S.; Kioupakis, E. Quasiparticle band structure and optical properties of rutile GeO_2, an ultra-wide-band-gap semiconductor. *J. Appl. Phys.* **2019**, *126* (8), No. 085703.
(12) Bushick, K.; Mengle, K. A.; Chae, S.; Kioupakis, E. Electron and hole mobility of rutile GeO_2 from first principles: An ultrawide-bandgap semiconductor for power electronics. *Appl. Phys. Lett.* **2020**, *117* (18), No. 182104.
(13) Chae, S.; Mengle, K.; Lu, R.; Olvera, A.; Sanders, N.; Lee, J.; Poudeu, P.; Heron, J.; Kioupakis, E. Thermal conductivity of rutile germanium dioxide. *Appl. Phys. Lett.* **2020**, *117* (10), No. 102106.
(14) Chae, S.; Lee, J.; Mengle, K. A.; Heron, J. T.; Kioupakis, E. Rutile GeO_2: An ultrawide-band-gap semiconductor with ambipolar doping. *Appl. Phys. Lett.* **2019**, *114* (10), No. 102104.
(15) Niedermeier, C. A.; Ide, K.; Katase, T.; Hosono, H.; Kamiya, T. Shallow valence band of rutile GeO_2 and P-type doping. *J. Phys. Chem. C* **2020**, *124* (47), 25721−25728.
(16) Lyons, J. L. Self-trapped holes and polaronic acceptors in ultrawide-bandgap oxides. *J. Appl. Phys.* **2022**, *131* (2), No. 025701.
(17) Lyons, J. L.; Janotti, A. A p-type dopable ultrawide-bandgap oxide. *J. Phys.: Condens. Matter* **2024**, *36* (8), No. 085501.
(18) Deng, G.; Huang, Y.; Chen, Z.; Saito, K.; Tanaka, T.; Arita, M.; Guo, Q. Heteroepitaxy of (100)-oriented rutile GeO_2 film on *c*-plane sapphire by pulsed laser deposition. *Mater. Lett.* **2022**, *326*, No. 132945.
(19) Nalam, P. G.; Das, D.; Tan, S.; Ramana, C. V. Controlled phase stabilization enabled tunable optical properties of nanocrystalline GeO_2 films. *ACS Applied Electronic Materials* **2022**, *4* (6), 3115−3124.
(20) Takane, H.; Kakeya, I.; Izumi, H.; Wakamatsu, T.; Isobe, Y.; Kaneko, K.; Tanaka, K. Low-temperature electron transport of rutile-type $Ge_xSn_{1-x}O_2$. *J. Appl. Phys.* **2023**, *134* (16), No. 165706.
(21) Rahaman, I.; Ellis, H. D.; Anderson, K.; Scarpulla, M. A.; Fu, K. Growth of GeO_2 on *R*-plane and *C*-plane Sapphires by MOCVD. *ACS Applied Engineering Materials* **2024**, *2* (6), 1724−1736.
(22) Rahaman, I.; Duersch, B. G.; Ellis, H. D.; Scarpulla, M. A.; Fu, K. Epitaxial growth of rutile GeO_2 via MOCVD. *Appl. Phys. Lett.* **2024**, *125* (10), No. 102103.
(23) Takane, H.; Kaneko, K. High-Speed Growth of Epitaxial Rutile GeO_2 Thin Film on (001) TiO_2 Under Highly Oxygen-Rich Condition and Its Structural Analysis; *Electrochemical Society Meeting Abstracts*; The Electrochemical Society, Inc.: 2021; pp 1902−1902.
(24) Chae, S.; Pressley, L. A.; Paik, H.; Gim, J.; Werder, D.; Goodge, B. H.; Kourkoutis, L. F.; Hovden, R.; McQueen, T. M.; Kioupakis, E.; Heron, J. T. Germanium dioxide: A new rutile substrate for epitaxial film growth. *Journal of Vacuum Science Technology A* **2022**, *40* (5), No. 050401.
(25) Chae, S.; Paik, H.; Vu, N.; Kioupakis, E.; Heron, J. Epitaxial stabilization of rutile germanium oxide thin film by molecular beam epitaxy. *Appl. Phys. Lett.* **2020**, *117* (7), No. 072105.
(26) Liu, F.; Truttmann, T. K.; Lee, D.; Matthews, B. E.; Laraib, I.; Janotti, A.; Spurgeon, S. R.; Chambers, S. A.; Jalan, B. Hybrid molecular beam epitaxy of germanium-based oxides. *Communications Materials* **2022**, *3* (1), 69.
(27) Chen, W.; Egbo, K.; Tornatzky, H.; Ramsteiner, M.; Wagner, M. R.; Bierwagen, O. In situ study and modeling of the reaction kinetics during molecular beam epitaxy of GeO_2 and its etching by Ge. *APL Materials* **2023**, *11* (7), No. 071110.
(28) Angell, C. A. Formation of glasses from liquids and biopolymers. *Science* **1995**, *267* (5206), 1924−1935.
(29) Lamoreaux, R.; Hildenbrand, D.; Brewer, L. High-Temperature Vaporization Behavior of Oxides II. Oxides of Be, Mg, Ca, Sr, Ba, B, Al, Ga, In, Tl, Si, Ge, Sn, Pb, Zn, Cd, and Hg. *Journal of physical and chemical reference data* **1987**, *16* (3), 419−443.
(30) Wang, T.; Prakash, A.; Warner, E.; Gladfelter, W. L.; Jalan, B. Molecular beam epitaxy growth of SnO_2 using a tin chemical precursor. *Journal of Vacuum Science & Technology A* **2015**, *33* (2), No. 020606.
(31) Barin, I.; Platzki, G. *Thermochemical Data of Pure Substances*; VCH: 1989; Vol. *304*, p 117.
(32) Shimazaki, E.; Matsumoto, N.; Niwa, K. The vapor pressure of germanium dioxide. *Bull. Chem. Soc. Jpn.* **1957**, *30* (9), 969−971.
(33) Durben, D. J.; Wolf, G. H. Raman spectroscopic study of the pressure-induced coordination change in GeO_2 glass. *Phys. Rev. B* **1991**, *43* (3), 2355.
(34) Richet, P. GeO_2 vs SiO_2: Glass transitions and thermodynamic properties of polymorphs. *Physics and chemistry of minerals* **1990**, *17* (1), 79−88.

https://doi.org/10.1021/acs.nanolett.4c05043
Nano Lett. 2025, 25, 299−305